separations

MDPI

Article

Identifying Accessible Ag^+ Sites as the Key Active Sites Governing Xenon Capture in Ag-Exchanged FAU Zeolite

Yuqiang Sheng [1], Yongzhen Zhang [2], Shujiang Liu [1], Zhanying Chen [1], Di Liu [2,*] and Shilian Wang [1,*]

[1] CTBT Beijing National Data Centre and Beijing Radionuclide Laboratory, Beijing 100085, China
[2] School of Chemical and Environmental Engineering, China University of Mining & Technology-Beijing, Beijing 100083, China
* Correspondence: liudi0713@163.com (D.L.); shilian.wang@nrl.org.cn (S.W.)

Abstract

To address the challenge of identifying the true structure–performance relationship governing xenon adsorption in silver-exchanged zeolites, a series of Ag/13X adsorbents with tunable silver loadings were synthesized via liquid-phase ion exchange. The unique FAU-type topology of 13X zeolite, composed of spacious supercages interconnected by large 12-membered-ring windows, enables high silver dispersion while minimizing diffusion limitations. This unique structural advantage makes Ag/13X an ideal model system for investigating the intrinsic role of silver active sites in Xe adsorption. We identify a pronounced volcano-shaped dependence of Xe adsorption on silver loading, establishing that total silver content is not the governing factor for Xe capture. Combined structural characterization and spectroscopic analyses reveal that increasing silver loading continuously alters silver speciation from highly dispersed Ag^+ ions toward more aggregated silver species, which may reduce the fraction of accessible Ag^+-related adsorption sites and simultaneously modify the local electronic environment of silver species. At an optimal $AgNO_3$ exchange concentration of 0.5 M, the predominance of well-dispersed Ag^+ species maximizes accessible active-site density and leads to the highest Xe uptake. Charge-corrected GCMC simulations provide molecular-level validation by showing that these accessible Ag^+ sites reinforce Xe adsorption through stronger ion-induced dipole interactions. Consequently, this work identifies the density of accessible Ag^+ sites as an important descriptor for Xe capture, offering a design guideline for engineering high-efficiency noble-gas adsorbents.

Keywords: xenon capture; Ag-exchanged 13X zeolite; accessible Ag^+ sites; silver speciation; GCMC simulation

Academic Editor: Gavino Sanna

Received: 29 August 2026
Revised: 11 September 2026
Accepted: 15 September 2026
Published: 17 September 2026

1. Introduction

Xenon (Xe) is a strategically important noble gas with critical applications in semiconductor manufacturing, microelectronics, deep-space ion propulsion, and nuclear medical imaging [1]. However, its ultralow concentration in industrial off-gases, combined with the presence of krypton (Kr) and other impurities, renders its efficient recovery technically challenging and economically demanding [2–5]. Compared with conventional energy-intensive cryogenic distillation, pressure swing adsorption (PSA) based on porous adsorbents has emerged as a promising alternative owing to its lower energy consumption and simpler process design [6–8]. Among various porous adsorbents, zeolites have attracted considerable attention because of their high structural stability, well-defined pore architectures, and readily tunable ion-exchange chemistry.

Despite these advantages, the intrinsic interaction between the aluminosilicate framework of zeolites and Xe is relatively weak, resulting in limited adsorption affinity. To strengthen Xe-adsorbent interactions, silver species have been widely incorporated into zeolites through ion exchange, leading to substantially enhanced Xe adsorption [9–16]. However, the identity of the silver species primarily responsible for Xe adsorption remains under debate. Isolated Ag^+ ions, partially reduced silver species, and small silver clusters have all been proposed as the dominant adsorption sites, yet no clear consensus has been established [12–15]. A key reason for this inconsistency is that increasing silver loading can simultaneously alter silver speciation, active-site accessibility, and pore structure [17–19]. These closely coupled changes make it difficult to distinguish the intrinsic contribution of silver active sites from changes in pore accessibility and transport-related effects, thereby obscuring the underlying structure–performance relationship governing Xe adsorption in silver-exchanged zeolites.

Addressing this challenge requires a suitable model system in which the intrinsic role of silver active sites can be examined with minimal interference from pore blockage and diffusion limitations. In this regard, 13X zeolite with the FAU topology is particularly well suited. Its spacious supercages (~1.12 nm), interconnected by large 12-membered-ring windows (~0.74 nm), provide abundant adsorption space and facilitate molecular transport. More importantly, compared with narrow-pore zeolites, where silver incorporation can readily cause severe pore blockage and diffusion limitations, the open FAU framework can accommodate substantial amounts of silver species while largely preserving pore accessibility. This structural advantage makes Ag/13X a well-defined model platform for distinguishing intrinsic active-site effects from transport-related limitations and thus for more clearly identifying the factors governing Xe adsorption. However, systematic studies that distinguish the contributions of these closely associated effects remain limited, leaving the underlying structure–performance relationship governing Xe adsorption insufficiently understood.

Herein, a series of Ag/13X zeolites with systematically varied silver loadings was prepared via liquid-phase ion exchange. By integrating structural and spectroscopic characterization with Xe adsorption measurements, thermodynamic analysis, and charge-corrected Grand Canonical Monte Carlo (GCMC) simulations, we establish the relationship between silver speciation, accessible Ag^+ sites, and Xe adsorption performance. A pronounced volcano-shaped dependence of Xe uptake on silver loading is identified, revealing that Xe adsorption is not governed simply by the total silver content but is strongly influenced by the density of accessible Ag^+ sites. Moreover, the open FAU pore network largely preserves pore accessibility, helping to reduce transport-related interference and facilitate the utilization of accessible Ag^+ sites. These findings clarify the structure–performance relationship governing Xe adsorption in Ag/13X and highlight active-site accessibility as an important design parameter for high-performance noble-gas adsorbents.

2. Materials and Methods

2.1. Preparation of Ag/13X Zeolites

Ag-loaded 13X zeolites with different silver loadings were prepared via a liquid-phase ion-exchange method using commercial 13X zeolite (Nankai University Catalyst Factory, Tianjin, China) as the support. $AgNO_3$ aqueous solutions (Sinopharm Chemical Reagent Co., Ltd., Shanghai, China) with concentrations of 0.1, 0.5, and 1.0 M were prepared separately. The ion-exchange process was conducted at a liquid-to-solid ratio of 20:1 (20 mL solution per gram of zeolite). Specifically, 13X zeolite was added to the $AgNO_3$ solution and stirred at 45 °C in a thermostatic water bath under dark conditions for 2 h. The ion-exchange procedure was repeated twice to ensure sufficient incorporation of silver species.

After ion exchange, the solid products were separated by vacuum filtration and thoroughly washed with deionized water to remove residual silver salts. The obtained samples were dried at 60 °C for 12 h and subsequently calcined in air at 425 °C for 3 h. The resulting samples were denoted as 0.1 MAg/13X, 0.5 MAg/13X, and 1 MAg/13X, respectively. The preparation procedure of Ag/13X zeolites is illustrated in Figure 1.

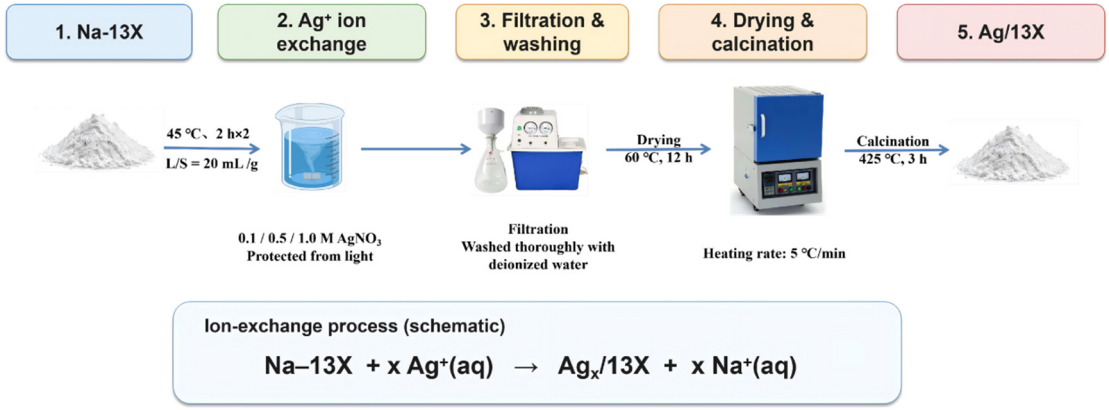

Figure 1. Schematic illustration of the preparation procedure for Ag/13X zeolites via Ag^+ ion exchange.

2.2. Characterization

The crystal structures of the samples were characterized by X-ray diffraction (XRD) using a SmartLab SE (2038) diffractometer (Rigaku Corporation, Akishima, Tokyo, Japan) equipped with Cu Kα radiation (λ = 1.5406 Å). Diffraction patterns were collected over a 2θ range of 5–50° at a scanning rate of 10°/min. X-ray fluorescence (XRF) analysis was performed using a Malvern Panalytical Axios spectrometer (Malvern Panalytical, Almelo, The Netherlands) equipped with a 4 kW Rh-anode X-ray tube. Approximately 2 g of powder was pressed into a pellet (~40 mm in diameter) at 30 tons for 30 s, with boric acid (Sinopharm Chemical Reagent Co., Ltd., Shanghai, China) used as a backing material when necessary. Measurements were conducted under vacuum using SuperQ software (version 5.0) with the Omnian standardless analysis program and LiF200 (60 kV, 60 mA), PET (30 kV, 120 mA), and Ge (30 kV, 120 mA) analyzing crystals. The morphology and microstructure of the samples were examined using a field-emission scanning electron microscope (SEM, GeminiSEM 300, Carl Zeiss Microscopy GmbH, Jena, Germany). Nitrogen adsorption–desorption isotherms were measured at 77 K using a BSD-660S A3S physical adsorption analyzer (BSD Instrument Technology (Beijing) Co., Ltd., Beijing, China). Prior to analysis, all samples were degassed under vacuum at 200 °C for 2 h. The Brunauer–Emmett–Teller (BET) specific surface area was calculated using the multipoint BET method, while the micropore volume was determined by the t-plot method. Ultraviolet-visible diffuse reflectance spectra (UV-Vis DRS) were recorded on a UH4150 UV-Vis-NIR spectrophotometer (Hitachi High-Tech Corporation, Tokyo, Japan) in the wavelength range of 200–800 nm using $BaSO_4$ supplied by the testing facility as the reference material. The surface elemental composition and chemical states of the samples were analyzed by X-ray photoelectron spectroscopy (XPS) using a K-Alpha spectrometer (Thermo Scientific, Waltham, MA, USA) equipped with a monochromatic Al Kα X-ray source (hν = 1486.6 eV). The binding energies were calibrated using the C 1s peak at 284.8 eV as the reference. Static Xe adsorption isotherms were measured using a BK200C surface area and pore size analyzer (Beijing JWGB Sci. & Tech. Co., Ltd., Beijing, China) at 298 K over a pressure range of 0–1 bar. Approximately 0.2 g of each sample was used for each measurement. The mass of each sample was determined by weighing the empty

sample tube and the sample-loaded tube using a CP225D analytical balance (Sartorius, Göttingen, Germany) and calculating the difference. Prior to adsorption measurements, the samples were degassed under vacuum at 250 °C for 12 h to remove physically adsorbed water and other residual gases from the pores. After degassing, the sample tube was cooled to room temperature and transferred to the analysis station maintained at 298 K using a thermostatic bath. Ultra-high-purity Xe (99.999%; Sichuan Runtai Specialty Gas Co., Ltd., Guanghan, China) was used as the adsorbate without a carrier gas. Because a static volumetric adsorption method was employed, no continuous gas flow rate or fixed adsorption time was involved. Xe was introduced stepwise, and the system was allowed to reach pressure and thermal equilibrium after each dosing step. The equilibrium pressure was automatically recorded by the instrument. The adsorption capacity was determined by the volumetric method and normalized to the mass of the adsorbent.

3. Results and Discussion

3.1. Crystal Structure and Microstructural Analysis

To clarify the influence of $AgNO_3$ solution concentration on the chemical composition of the zeolite, the elemental compositions of a series of Ag/13X samples were analyzed by X-ray fluorescence spectroscopy (XRF), and the results are summarized in Table 1. The XRF results show that the Ag content progressively increased with increasing $AgNO_3$ concentration, accompanied by a corresponding decrease in the Na content, consistent with the progressive exchange of Ag^+ for Na^+ in 13X [20,21]. For 0.1 MAg/13X, the Ag content reached 6 mol%, while 4 mol% Na remained, indicating incomplete Na^+/Ag^+ exchange under this condition. When the $AgNO_3$ concentration was increased to 0.5 M, the Na content decreased below the detection level, while further increasing the concentration to 1.0 M resulted in only a slight increase in the Ag content from 10 mol% to 11 mol%, suggesting that the ion-exchange process had approached saturation. The Si/Al ratios derived from XRF varied slightly between 1.23 and 1.38 but showed no systematic dependence on the $AgNO_3$ concentration. In particular, the absence of a progressive increase in the Si/Al ratio with increasing $AgNO_3$ concentration indicates that no significant framework dealumination was detectable during the ion-exchange treatment, within the limits of XRF precision.

Table 1. Elemental composition of Ag/13X samples determined by XRF analysis.

Sample	Elemental Content (mol%)					Elemental Molar Ratio	
	Na	Ag	Si	Al	O	Molar Ratio Ag/(Ag + Na)	Si/Al
13X	15	0	16	13	56	0	1.23
0.1 MAg/13X	4	6	18	13	59	0.6	1.38
0.5 MAg/13X	0	10	17	13	60	1	1.31
1 MAg/13X	0	11	17	13	59	1	1.31

To investigate the influence of $AgNO_3$ concentration on the crystalline phase, framework integrity, and possible formation of crystalline silver species in Ag/13X zeolites, XRD patterns of the Ag-modified samples were collected, as shown in Figure 2a. All Ag/13X samples exhibited the characteristic diffraction peaks of FAU-type zeolite, which were consistent with the standard 13X zeolite pattern (PDF#38-0237), indicating that the FAU framework was well preserved after Ag^+ ion exchange [20]. The major diffraction peaks were indexed to the corresponding crystallographic planes, as shown in Figure 2a. With increasing $AgNO_3$ concentration, the diffraction peak intensity showed a slight decrease, whereas no obvious peak shift or disappearance of the characteristic reflections was observed. This suggests that Ag incorporation had only a limited influence on the

long-range crystalline structure of 13X zeolite. According to previous reports, the decrease in diffraction intensity after metal-ion exchange is generally associated with local structural rearrangement, redistribution of extra-framework cations, and changes in scattering contrast, rather than framework collapse [22–25]. Together with the absence of a systematic increase in the XRF-derived Si/Al ratio, these results provide no clear evidence for significant framework dealumination during the ion-exchange treatment. In addition, no diffraction peaks corresponding to metallic Ag were detected at $2\theta \approx 38.1^\circ$ and 44.3°, implying that crystalline Ag nanoparticles were absent or present in amounts below the detection limit of XRD [26,27].

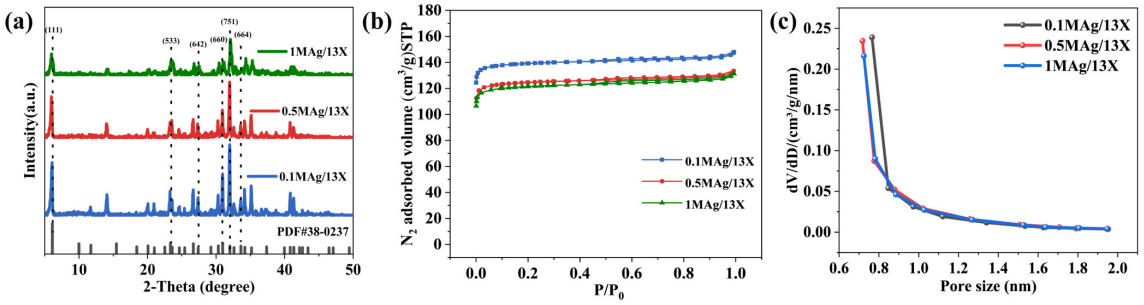

Figure 2. XRD patterns (**a**), N_2 adsorption–desorption isotherms (**b**), and pore size distributions (**c**) of Ag/13X samples. The dashed lines in (**a**) indicate the positions of the characteristic diffraction peaks of the FAU framework.

To further evaluate whether Ag incorporation affected the pore structure of Ag/13X zeolites, N_2 adsorption–desorption measurements were performed, and the corresponding results are summarized in Table 2. As shown in Figure 2b, all Ag/13X samples exhibited typical Type I adsorption isotherms, indicating that the microporous characteristics of the FAU framework were largely retained after Ag^+ ion exchange [28]. Compared with pristine 13X, the Ag/13X samples exhibited lower BET surface areas and pore volumes, consistent with partial occupation of the microporous space by introduced Ag species. Within the Ag/13X series, the BET surface area and pore volume decreased further with increasing $AgNO_3$ concentration. Meanwhile, the average pore diameters of the Ag/13X samples remained in the range of 0.72–0.77 nm, larger than the kinetic diameter of Xe molecules (~0.40 nm), suggesting that Xe molecules could still access the internal pore channels. Notably, 0.5 MAg/13X and 1 MAg/13X exhibited very similar porosity parameters, indicating that further increasing the $AgNO_3$ concentration from 0.5 to 1.0 M did not cause obvious additional pore loss. As expected from the structural design of the FAU framework, the large supercages and interconnected 12-membered-ring windows of 13X can accommodate relatively high amounts of Ag species while avoiding severe pore blockage. Therefore, these results confirm that the Ag/13X samples maintain sufficient pore accessibility, providing a suitable structural basis for further evaluating the influence of Ag species distribution and active-site accessibility on Xe adsorption [29].

Table 2. Textural properties of Ag/13X samples derived from N_2 adsorption–desorption measurements.

Sample	S_{BET} (m^2/g)	Total Pore Volume (cm^3/g)	t-Plot			H-K Average Pore Diameter (nm)
			S_{micro} (m^2/g)	$S_{external}$ (m^2/g)	V_{micro} (cm^3/g)	
13X	772.8	0.298	763.8	9.0	0.2868	0.6635
0.1 MAg/13X	571.1	0.228	559.7	11.4	0.2108	0.7653
0.5 MAg/13X	492.7	0.204	483.4	9.3	0.1895	0.7173
1 MAg/13X	488.3	0.200	474.8	13.5	0.1824	0.7241

Although XRD and N_2 adsorption analyses showed that the overall structure and pore characteristics were largely preserved after Ag modification, SEM and TEM were further used to examine the morphology and dispersion of silver species. As shown in the SEM images (Figure 3a–c), all Ag/13X samples retained the characteristic octahedral morphology of the parent 13X zeolite without obvious structural collapse or large silver aggregates on the external surface, indicating that the ion-exchange process did not significantly alter the overall morphology of the zeolite crystals. To gain further insight into the distribution of silver species, TEM observations (Figure 3d–f) and EDS elemental mapping analyses (Figure 4) were performed. TEM images show no obvious large nanoparticles or aggregates on the zeolite surface, suggesting that extensive large-scale Ag aggregation did not occur after ion exchange and subsequent calcination. This observation is consistent with the XRD results, in which no diffraction peaks attributable to crystalline metallic Ag were detected. Furthermore, EDS elemental mapping shows that Ag is broadly distributed throughout the zeolite crystals (Figure 4), indicating that Ag species were successfully introduced into the 13X zeolite during ion exchange.

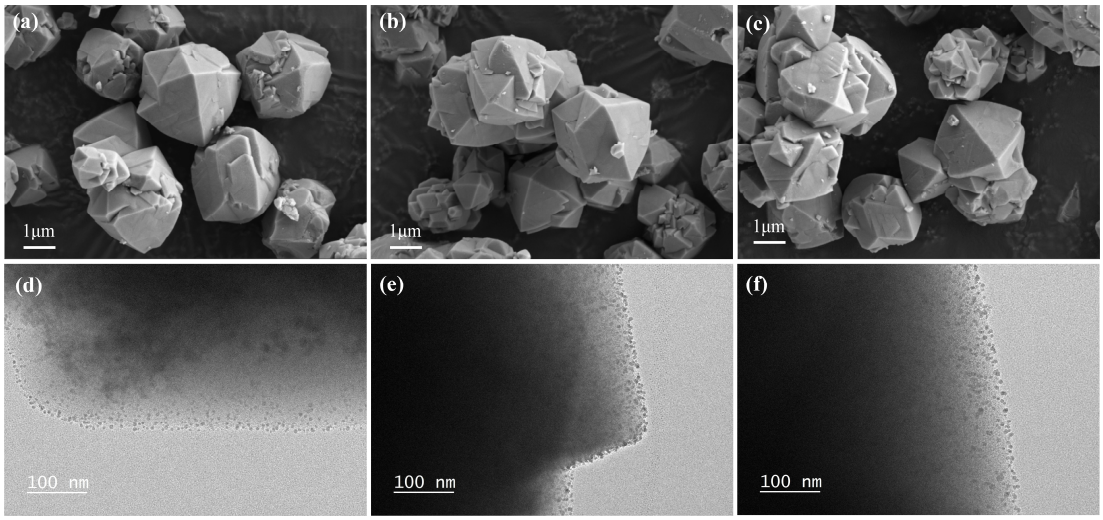

Figure 3. SEM images of (**a**) 0.1 MAg/13X, (**b**) 0.5 MAg/13X, and (**c**) 1 MAg/13X, and TEM images of (**d**) 0.1 MAg/13X, (**e**) 0.5 MAg/13X, and (**f**) 1 MAg/13X.

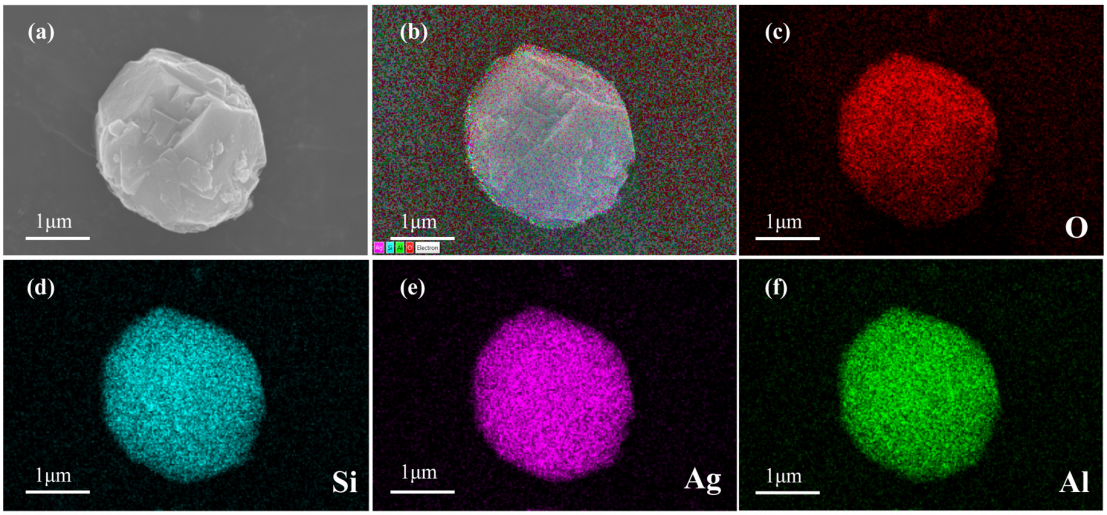

Figure 4. SEM image and corresponding EDS elemental mapping images of 1MAg/13X zeolite: SEM image (**a**); merged elemental mapping image (**b**); O (**c**, red); Si (**d**, cyan); Ag (**e**, magenta); and Al (**f**, green).

To further investigate the chemical states of silver species, X-ray photoelectron spectroscopy (XPS) analysis was performed. The corresponding XPS survey spectra are presented in Figure S7. Because the binding energy difference between metallic Ag and ionic Ag species in the Ag 3d region is relatively small, the modified Auger parameter (α′) was employed to more reliably identify the silver oxidation states [30]. The modified Auger parameter is defined as the sum of the binding energy (BE) of the characteristic photoelectron peak (Ag $3d_{5/2}$) and the kinetic energy (KE) of the most intense Auger transition (Ag $M_4N_{45}N_{45}$), according to α′ = BE + KE. As a relative parameter, α′ effectively minimizes the influence of charging effects and other experimental factors that may shift absolute binding energies, thereby providing a more reliable assessment of the chemical state than the Ag 3d binding energy alone [31].

The Ag MNN Auger spectrum consists primarily of two major transitions, namely $M_4N_{45}N_{45}$ and M_5NN. Owing to the superposition of multiplet splitting and spin–orbit coupling effects associated with the M_4 and M_5 core levels, the Ag MNN spectrum exhibits a relatively complex line shape [30]. Therefore, only the α′ values calculated from the $M_4N_{45}N_{45}$ transition were considered in this work. As summarized in Table 3, the modified Auger parameter gradually increased from 723.1 to 723.5 eV with increasing silver loading. This trend suggests a gradual increase in the electron density surrounding silver species, indicating partial aggregation of isolated Ag^+ species and the formation of small silver clusters. Nevertheless, all α′ values remained substantially lower than that of metallic silver (≈726 eV), indicating that Ag^+ species remained dominant in all samples, while only limited amounts of silver clusters or metallic Ag species were present [32]. Although Ag^+ species remain dominant in all samples, increasing silver loading is accompanied by a greater contribution from aggregated Ag species, which may reduce the effective population of accessible Ag^+-related adsorption sites.

Table 3. Modified Auger parameters (α′) of 0.1 MAg/13X, 0.5 MAg/13X, and 1 MAg/13X samples.

Sample	BE(Ag $3d_{5/2}$) (eV)	KE(Ag MNN) (eV)	α′ (eV)
0.1 MAg/13X	368.5	354.6	723.1
0.5 MAg/13X	368.5	354.7	723.2
1 MAg/13X	368.6	354.9	723.5

Although XPS provides valuable information regarding the chemical state of silver, it cannot effectively distinguish the spatial distribution and aggregation state of silver species within the zeolite framework. Therefore, UV-Vis diffuse reflectance spectroscopy (UV-Vis DRS) was employed to further elucidate the evolution of silver species with increasing ion-exchange concentration (Figure 5c) [33]. Three characteristic absorption bands were observed in the UV-Vis spectra. The absorption band at approximately 223 nm is generally attributed to isolated Ag^+ species highly dispersed at exchange sites within the zeolite framework [34,35]. The band centered around 285 nm is assigned to small silver clusters, whereas the absorption feature at 339–348 nm is associated with larger silver clusters [36–38]. Combined with the XRF results, these observations reveal a clear evolution of silver species as the ion-exchange concentration increases. For the 0.1 MAg/13X sample, the silver species exhibited a high degree of dispersion; however, the overall silver loading remained relatively low according to XRF analysis, limiting the density of potential adsorption sites. Increasing the ion-exchange concentration to 0.5 M significantly enhanced the silver loading while maintaining silver species predominantly in the form of highly dispersed Ag^+ ions. In contrast, when the concentration was further increased to 1.0 M, only a marginal increase in total silver content was achieved, whereas substantial changes in silver speciation occurred. Specifically, the absorption band at approximately 339 nm, characteristic of larger silver clusters, became markedly stronger. Meanwhile, a pronounced

baseline elevation and absorption tail extending beyond 400 nm were observed. These spectral features indicate that excessive silver species tend to aggregate within the confined supercage environment of the FAU framework, suggesting the gradual evolution of highly dispersed Ag^+ species toward more aggregated Ag states [39–41].

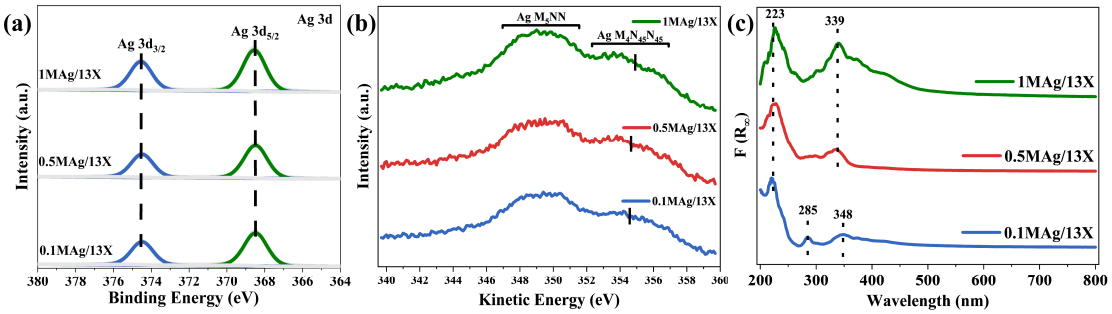

Figure 5. Ag 3d XPS spectra (**a**), Ag MNN Auger spectra (**b**), and UV-Vis DRS spectra (**c**) of 0.1 MAg/13X, 0.5 MAg/13X, and 1 MAg/13X samples. The dashed lines in (**a**,**c**) indicate the positions of the characteristic peaks.

The combined XRF, XPS, and UV-Vis DRS results indicate that an ion-exchange concentration of 0.5 M provides a favorable balance between silver loading and silver dispersion. This sample achieves a relatively high silver content while maintaining a large fraction of highly dispersed Ag^+ species, which is expected to favor a higher population of accessible Ag+-related adsorption sites and may preserve favorable local environments for Xe interaction. This Ag distribution is consistent with the enhanced Xe adsorption observed in the subsequent adsorption measurements.

3.2. Xenon Adsorption Performance and Isosteric Heat Analysis

To clarify how silver loading, silver speciation, and active-site accessibility affect Xe adsorption performance, Xe adsorption measurements were conducted for Ag/13X zeolites at 298 K. As shown in Figure 6a, all Ag-modified samples exhibited significantly enhanced Xe adsorption capacities compared with pristine 13X over the entire pressure range. The overall adsorption capacity followed the order of 13X < 0.1 MAg/13X < 1 MAg/13X < 0.5 MAg/13X, with 0.5 MAg/13X showing the highest Xe uptake of approximately 58 cm^3/g at 100 kPa. The Xe adsorption capacity did not increase monotonically with increasing silver loading, but instead exhibited a clear volcano-type dependence on the $AgNO_3$ exchange concentration. For 0.1 MAg/13X, although Ag species were highly dispersed and Ag^+ species were dominant, the relatively low silver content limited the number of available adsorption sites. Increasing the exchange concentration to 0.5 M substantially increased the population of highly dispersed Ag^+ species while maintaining good site accessibility within the interconnected FAU pore network, leading to the highest Xe adsorption capacity. In contrast, further increasing the $AgNO_3$ concentration to 1.0 M resulted in only a marginal increase in the total silver content, while UV-Vis DRS revealed a greater contribution from aggregated Ag species. 0.5 MAg/13X and 1 MAg/13X exhibited very similar textural parameters, suggesting that substantial additional pore loss is unlikely to be the dominant origin of the decreased Xe uptake. Instead, the decline in adsorption is consistent with the evolution of Ag speciation from highly dispersed ionic species toward more aggregated states. Such aggregation may influence Xe adsorption through two possible effects: reducing the population of accessible Ag^+-related adsorption sites and modifying the intrinsic Xe–Ag interaction through changes in the electronic and geometric environment of silver species. Previous theoretical studies have also shown that

the interaction between Xe and Ag species is sensitive to the aggregation state of silver [15], supporting the importance of Ag speciation in determining Xe adsorption behavior.

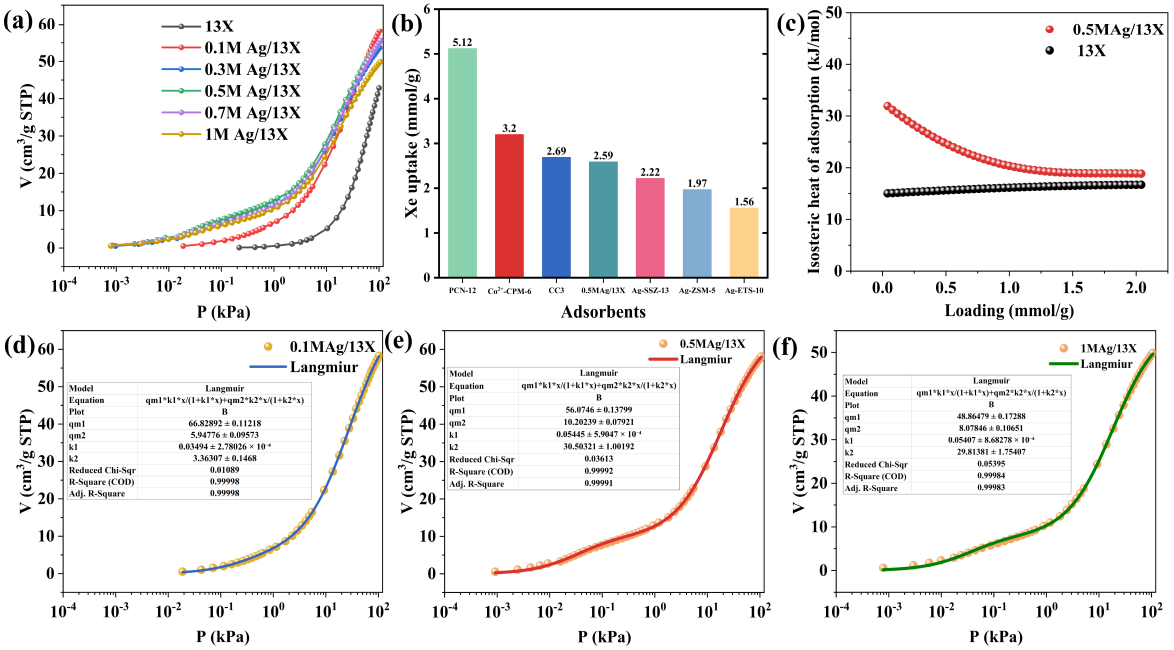

Figure 6. (**a**) Xe adsorption isotherms of pristine 13X and a series of Ag/13X samples. (**b**) Comparison of Xe adsorption capacities of 0.5 MAg/13X with representative Xe adsorbents reported in the literature. (**c**) Isosteric heats of Xe adsorption for 13X and 0.5 MAg/13X. (**d**–**f**) Dual-site Langmuir model fitting of Xe adsorption isotherms for 0.1 MAg/13X, 0.5 MAg/13X, and 1 MAg/13X, respectively.

The adsorption performance of the optimized 0.5 MAg/13X sample was further compared with representative Xe adsorbents reported in the literature. As shown in Figure 6b, 0.5 MAg/13X exhibits a Xe adsorption capacity of approximately 2.59 mmol/g at 298 K and 100 kPa, showing competitive performance among representative Xe adsorbents. For the Ag/13X system, the favorable adsorption performance can be attributed to the combination of the spacious FAU supercage structure, large 12-membered-ring windows, and the optimized distribution of accessible Ag-related adsorption sites, which provide sufficient adsorption space, facilitate Xe diffusion, and improve the utilization of silver active sites.

To further clarify the thermodynamic nature of Xe adsorption, adsorption isotherms measured at different temperatures were fitted using the Virial equation, and the corresponding isosteric heats of adsorption were calculated as a function of Xe loading [42,43]. As shown in Figure 6c, the initial isosteric heat of adsorption for 0.5 MAg/13X was approximately 32 kJ/mol, which was much higher than that of pristine 13X, approximately 15 kJ/mol. This increase indicates that the introduced silver species create high-affinity adsorption sites and strengthen the interaction between Xe and the adsorbent. Moreover, the Q_{st} value of 0.5 MAg/13X decreased rapidly with increasing Xe loading, indicating the preferential occupation of strong silver-associated adsorption sites at low coverage, followed by adsorption on weaker framework sites at higher coverage.

The Xe adsorption isotherms of Ag/13X samples were further fitted using a dual-site Langmuir model to quantitatively analyze the heterogeneous adsorption behavior [44–46]. As shown in Figure 6d–f, all samples were well described by the dual-site Langmuir model, with high correlation coefficients, suggesting the coexistence of weak and strong adsorption sites in the Ag-modified zeolites. The weak adsorption sites are mainly associated with nonspecific physisorption within the zeolite framework, whereas the strong adsorption

sites are related to Xe interactions with silver species. Compared with 0.1 MAg/13X, 0.5 MAg/13X showed higher capacity and affinity for the strong adsorption sites, indicating that the 0.5 M ion-exchange condition increases the number of high-affinity sites and strengthens their interaction with Xe. These results further support the important role of accessible Ag^+ species in the enhanced Xe adsorption performance of Ag/13X zeolites.

The Xe adsorption behavior can be related to the structural and surface properties of Ag/13X. XRD and N_2 adsorption results show that the FAU framework and pore accessibility are largely preserved after Ag ion exchange, while spectroscopic analyses reveal that 0.5 MAg/13X maintains a high proportion of highly dispersed Ag^+ species, whereas further increasing the Ag loading promotes Ag aggregation. This evolution may reduce the effective population of highly dispersed and accessible Ag^+-related adsorption sites and may also modify the intrinsic Xe-Ag affinity through changes in the electronic and geometric environment of the Ag species, with both effects potentially contributing to the lower Xe uptake. Combined with the isosteric heat analysis, these results indicate that the open FAU pore network maintains Xe accessibility, while Ag speciation plays an important role in determining the adsorption affinity and capacity.

The recyclability of 0.5 MAg/13X was further evaluated through repeated Xe adsorption–desorption cycles. As shown in Figure 7, the adsorption isotherms remained nearly unchanged over five consecutive cycles, indicating good cycling stability and regeneration performance. The structural stability after Xe adsorption was further supported by XRD, FTIR, and SEM characterization (Figure S8). These results show that 0.5 MAg/13X maintains both its adsorption performance and structural integrity during repeated Xe adsorption–desorption processes.

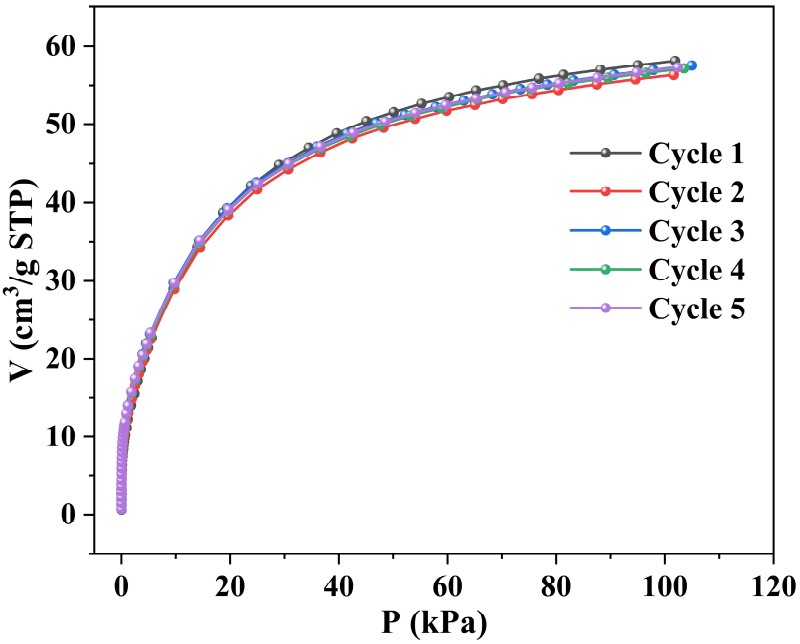

Figure 7. Xe adsorption isotherms of 0.5 MAg/13X over five consecutive adsorption–desorption cycles at 298 K.

3.3. GCMC Simulation

A modified grand canonical Monte Carlo (GCMC) model was employed to investigate the molecular-level adsorption behavior and evaluate the role of Ag^+-induced polarization in Xe adsorption on Ag/13X zeolites [47]. The crystal structure of the Ag/13X model used for the simulations is shown in Figure S9. Initially, simulations based on the default parameters of the COMPASS and Universal force fields significantly underestimated the

experimental Xe adsorption capacity and failed to reproduce the enhanced adsorption affinity after silver incorporation. This discrepancy may arise from the limitations of conventional Lennard-Jones-based force fields, which cannot explicitly describe the ion-induced dipole interaction between Ag^+ species and Xe atoms. Therefore, polarization-related interactions should be considered when modeling Xe adsorption in Ag-containing zeolites. To partially compensate for the missing polarization effect, an empirical effective charge of −0.09 e was assigned to Xe atoms, while the parameters of the zeolite framework and silver species were kept unchanged. It should be emphasized that this effective charge does not represent the actual charge state of Xe. Instead, it serves as a simplified correction to enhance the electrostatic contribution and approximate the polarization of Xe induced by the strong local electric field around Ag^+ sites. As shown in Figure 8, the charge-corrected model more closely reproduced the experimental adsorption isotherm than the uncorrected force-field models over the entire pressure range, supporting the importance of polarization-related interactions in Xe adsorption on Ag-exchanged zeolites. The remaining deviations between the simulated and experimental adsorption capacities may arise because the model does not explicitly account for the heterogeneous distribution of silver species, local variations in electrostatic fields, or the dynamic polarization of Xe within zeolite pores. The modified GCMC model captures the experimental adsorption trend and supports the proposed role of highly dispersed Ag^+ species in enhancing Xe adsorption through ion-induced dipole interactions.

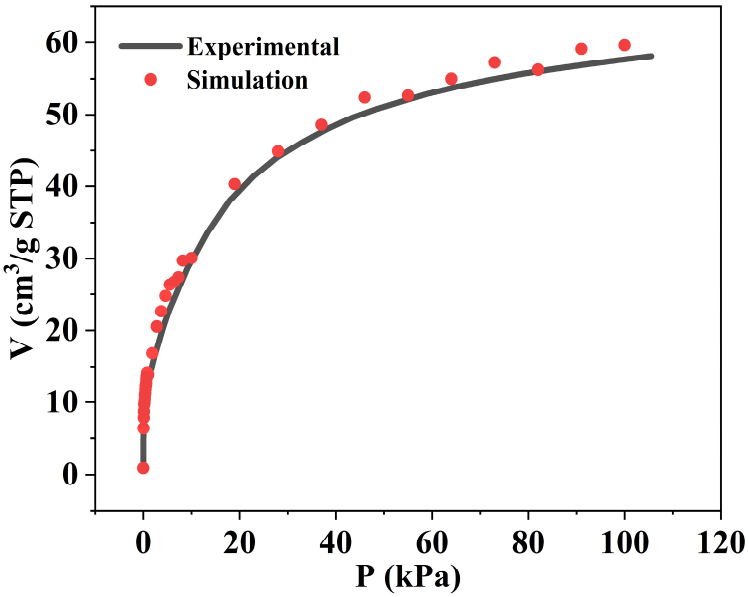

Figure 8. Experimental and GCMC-simulated Xe adsorption isotherms of 0.5 MAg/13X.

4. Conclusions

In summary, this work reveals that Xe adsorption in Ag-exchanged 13X zeolites is strongly influenced by the density of accessible Ag^+ active sites rather than the total silver loading. Moderate silver loading maximizes the population of highly dispersed Ag^+-related adsorption sites, whereas excessive silver incorporation promotes the formation of more aggregated Ag species. This aggregation may decrease site accessibility and alter the local Xe–Ag interaction environment, both of which could contribute to the reduced adsorption performance. Thermodynamic analysis together with charge-corrected GCMC simulations demonstrates that these accessible Ag^+ sites strengthen Xe adsorption through enhanced ion-induced dipole interactions, while the spacious FAU topology ensures their efficient utilization by minimizing transport limitations. By identifying accessible Ag^+

site density as an important descriptor for Xe adsorption in silver-exchanged zeolites, this work establishes a mechanistic foundation and a rational design principle for optimizing noble-gas adsorbents beyond simply increasing silver loading.

Supplementary Materials: The following supporting information can be downloaded at: https://www.mdpi.com/article/10.3390/separations13090266/s1, Figure S1: XRD pattern of the parent 13X zeolite. The characteristic diffraction peaks are consistent with the standard FAU-type zeolite (PDF#38-0237), confirming that the pristine 13X possesses a well-defined FAU framework prior to Ag^+ ion exchange; Figure S2: N_2 adsorption–desorption isotherm of the pristine 13X zeolite measured at 77 K; Figure S3: SEM images of 13X recorded at different magnifications, with scale bars of (a) 20 μm, (b) 10 μm, (c) 2 μm, and (d) 1 μm; Figure S4: SEM images of 0.5MAg/13X recorded at different magnifications, with scale bars of (a) 20 μm, (b) 10 μm, (c) 2 μm, and (d) 1 μm; Figure S5: TEM images of 13X recorded at different magnifications, with scale bars of (a) 500 nm, (b) 200 nm, (c) 100 nm, and (d) 50 nm; Figure S6: TEM images of 0.5MAg/13X recorded at different magnifications, with scale bars of (a) 500 nm, (b) 200 nm, (c) 100 nm, and (d) 50 nm; Figure S7: XPS survey spectra of (a) 0.1MAg/13X, (b) 0.5MAg/13X, and (c) 1MAg/13X; Figure S8: Structural characterization of Ag/13X before and after Xe adsorption. (a) XRD patterns and (b) FTIR spectra of fresh and Xe-adsorbed Ag/13X; SEM images of (c) fresh Ag/13X and (d) Xe-adsorbed Ag/13X; Supplementary Method: Construction of the GCMC Model and Simulation Method; Figure S9: Crystal structure of the Ag/13X model used for the GCMC simulations. The model was derived from the FAU framework and contains 83 Ag^+ ions distributed within the pore system; Table S1: Elemental composition (wt.%) of 13X and Ag/13X samples determined by XRF.

Author Contributions: Conceptualization, D.L. and S.W.; methodology, Y.Z.; investigation, Y.S., Y.Z., S.L. and Z.C.; validation, S.L.; formal analysis, Y.S. and Y.Z.; resources, Z.C.; data curation, Y.S.; visualization, Y.S. and Y.Z.; writing—original draft preparation, Y.S. and Y.Z.; writing—review and editing, D.L. and S.W.; supervision, D.L. and S.W.; project administration, D.L. and S.W.; funding acquisition, S.W. All authors have read and agreed to the published version of the manuscript.

Funding: This research was funded by the Chinese National Science Foundation (12205126), Fundamental Research Funds for the Central Universities (2025ZKPYHH05), and National Key R&D Program of China (2024YFC2909804).

Data Availability Statement: The data supporting the findings of this study are available within the article and its Supplementary Materials.

Conflicts of Interest: The authors declare no conflicts of interest.

References

1. Banerjee, D.; Simon, C.M.; Elsaidi, S.K.; Haranczyk, M.; Thallapally, P.K. Xenon Gas Separation and Storage Using Metal-Organic Frameworks. *Chem* **2018**, *4*, 466–494. [CrossRef]
2. Banerjee, D.; Simon, C.M.; Plonka, A.M.; Motkuri, R.K.; Liu, J.; Chen, X.; Smit, B.; Parise, J.B.; Haranczyk, M.; Thallapally, P.K. Metal-Organic Framework with Optimally Selective Xenon Adsorption and Separation. *Nat. Commun.* **2016**, *7*, ncomms11831. [CrossRef] [PubMed]
3. Li, L.; Guo, L.; Zhang, Z.; Yang, Q.; Yang, Y.; Bao, Z.; Ren, Q.; Li, J. A Robust Squarate-Based Metal-Organic Framework Demonstrates Record-High Affinity and Selectivity for Xenon over Krypton. *J. Am. Chem. Soc.* **2019**, *141*, 9358–9364. [CrossRef] [PubMed]
4. Gueibe, C.; Rutten, J.; Camps, J.; Moyaux, D.; Schroeyers, W.; Plenteda, R.; Hermanspahn, N.; Minta, D.; Schreurs, S. Silver-Exchanged Zeolites for Collecting and Separating Xenon Directly from Atmospheric Air. *Sep. Purif. Technol.* **2023**, *323*, 124433. [CrossRef]
5. Simon, C.M.; Mercado, R.; Schnell, S.K.; Smit, B.; Haranczyk, M. What Are the Best Materials To Separate a Xenon/Krypton Mixture? *Chem. Mater.* **2015**, *27*, 4459–4475. [CrossRef]
6. Bazan, R.E.; Bastos-Neto, M.; Moeller, A.; Dreisbach, F.; Staudt, R. Adsorption Equilibria of O_2, Ar, Kr and Xe on Activated Carbon and Zeolites: Single Component and Mixture Data. *Adsorption* **2011**, *17*, 371–383. [CrossRef]

7. Zhang, C.; Dong, X.; Chen, Y.; Wu, H.; Yu, L.; Zhou, K.; Wu, Y.; Xia, Q.; Wang, H.; Han, Y.; et al. Balancing Uptake and Selectivity in a Copper-Based Metal-Organic Framework for Xenon and Krypton Separation. *Sep. Purif. Technol.* **2022**, *291*, 120932. [CrossRef]
8. Zhao, Z.; Xiong, H.; Peng, Y.; Liu, X.; Wang, P.; Liu, J.; Deng, Z.; Chen, S.; Chen, J.; Zhou, Z.; et al. Pore Environment Modulation of Metal-Organic Frameworks Enables Efficient Adsorptive Separation of Xe/Kr. *Sep. Purif. Technol.* **2023**, *325*, 124529. [CrossRef]
9. Kuznicki, S.M.; Ansón, A.; Koenig, A.; Kuznicki, T.M.; Haastrup, T.; Eyring, E.M.; Hunter, D. Xenon Adsorption on Modified ETS-10. *J. Phys. Chem. C* **2007**, *111*, 1560–1562. [CrossRef]
10. Daniel, C.; Elbaraoui, A.; Aguado, S.; Springuel-Huet, M.-A.; Nossov, A.; Fontaine, J.-P.; Topin, S.; Taffary, T.; Deliere, L.; Schuurman, Y.; et al. Xenon Capture on Silver-Loaded Zeolites: Characterization of Very Strong Adsorption Sites. *J. Phys. Chem. C* **2013**, *117*, 15122–15129. [CrossRef]
11. Deliere, L.; Coasne, B.; Topin, S.; Gréau, C.; Moulin, C.; Farrusseng, D. Breakthrough in Xenon Capture and Purification Using Adsorbent-Supported Silver Nanoparticles. *Chem. Eur. J.* **2016**, *22*, 9660–9666. [CrossRef] [PubMed]
12. Deliere, L.; Topin, S.; Coasne, B.; Fontaine, J.-P.; De Vito, S.; Den Auwer, C.; Solari, P.L.; Daniel, C.; Schuurman, Y.; Farrusseng, D. Role of Silver Nanoparticles in Enhanced Xenon Adsorption Using Silver-Loaded Zeolites. *J. Phys. Chem. C* **2014**, *118*, 25032–25040. [CrossRef]
13. Oda, A.; Kouzai, H.; Sawabe, K.; Satsuma, A.; Ohkubo, T.; Gotoh, K.; Kuroda, Y. Orbital Trap of Xenon: Driving Force Distinguishing between Xe and Kr Found at a Single Ag(I) Site in MFI Zeolite at Room Temperature. *J. Phys. Chem. C* **2022**, *126*, 8312–8326. [CrossRef]
14. Coopersmith, K.J.; Broadwater, K.L.; Demers, S.M.E.; Monikandan, R.; Torcivia, M.; Roy, L.; Hunter, D. Investigating the Role of Silver Oxidation State on the Thermodynamic Interactions between Xenon and Silver-Functionalized Zeolites. *J. Phys. Chem. C* **2023**, *127*, 1598–1606. [CrossRef]
15. Nguyen, H.G.; Konya, G.; Eyring, E.M.; Hunter, D.B.; Truong, T.N. Theoretical Study on the Interaction between Xenon and Positively Charged Silver Clusters in Gas Phase and on the (001) Chabazite Surface. *J. Phys. Chem. C* **2009**, *113*, 12818–12825. [CrossRef]
16. Courtney, C.; Millet, A.; Couchaux, G.; Gossard, A.; Tuel, A.; Bonnet, N.; Topin, S.; Farrusseng, D. Toward Optimal Xenon Adsorption Capacity at Low Pressure on Silver-Exchanged Zeolites. *Ind. Eng. Chem. Res.* **2023**, *62*, 11939–11947. [CrossRef]
17. Li, Y.; Min, X.; Li, W.; Wang, Q.; Shang, M.; Yu, Y.; Tao, P.; Sun, T. Experimental and Computational Evaluation of Ag-Exchanged ZSM-5 and SSZ-13 for Xenon Capture. *Microporous Mesoporous Mater.* **2022**, *330*, 111631. [CrossRef]
18. Liu, S.; Lian, X.; Yue, B.; Xu, S.; Wu, G.; Chai, Y.; Zhang, Y.; Li, L. Control of Zeolite Local Polarity toward Efficient Xenon/Krypton Separation. *J. Am. Chem. Soc.* **2024**, *146*, 8335–8342. [CrossRef] [PubMed]
19. Torcivia, M.A.; Demers, S.M.E.; Broadwater, K.L.; Hunter, D.B. Investigating the Effects of Ag, Cu, and Pd Functionalized Chabazite on the Adsorption Affinities of Noble Gases Xe, Kr, and Ar. *J. Phys. Chem. C* **2023**, *127*, 3800–3807. [CrossRef]
20. Gęsikiewicz-Puchalska, A.; Zgrzebnicki, M.; Michalkiewicz, B.; Kałamaga, A.; Narkiewicz, U.; Morawski, A.W.; Wrobel, R. Changes in Porous Parameters of the Ion Exchanged X Zeolite and Their Effect on CO_2 Adsorption. *Molecules* **2021**, *26*, 7520. [CrossRef] [PubMed]
21. Phuong, N.T.; Huy, H.D.; Anh, L.M.N.; Duong, N.T.H.; Quang Long, N. Efficient Ethylene Removal of Silver-Exchanged Zeolite X for Fruit Preservation. *J. Ecol. Eng.* **2025**, *26*, 393–407. [CrossRef] [PubMed]
22. Tahraoui, Z.; Nouali, H.; Marichal, C.; Forler, P.; Klein, J.; Daou, T.J. Influence of the Compensating Cation Nature on the Water Adsorption Properties of Zeolites. *Molecules* **2020**, *25*, 944. [CrossRef] [PubMed]
23. Henao-Sierra, W.; Romero-Sáez, M.; Gracia, F.; Cacua, K.; Buitrago-Sierra, R. Water Vapor Adsorption Performance of Ag and Ni Modified 5A Zeolite. *Microporous Mesoporous Mater.* **2018**, *265*, 250–257. [CrossRef]
24. Guarnieri, G.D.P.; Laurenti, J.B.; Crespo, B.; Silva, E.B.; Maschio-Lima, T.; Júnior, V.S.; Goloni-Bertollo, E.M.; De Godoy, M.F.; De Almeida, M.T.G.; Nery, J.G. Nanometric Faujasite (FAU) Zeolite Ion-Exchanged with Metal Ions for Hemostatic and Antimicrobial Applications: A Thromboelastographic and Microbiological Study. *Chem. Asian J.* **2026**, *21*, e70755. [CrossRef] [PubMed]
25. Daou, T.J.; Dos Santos, T.; Nouali, H.; Josien, L.; Michelin, L.; Pieuchot, L.; Dutournie, P. Synthesis of FAU-Type Zeolite Membranes with Antimicrobial Activity. *Molecules* **2020**, *25*, 3414. [CrossRef] [PubMed]
26. Gicheva, G.; Panayotova, M.; Gemishev, O.; Kulinich, S.A.; Mintcheva, N. Silver Nanoparticles@Zeolite Composites: Preparation, Characterization and Antibacterial Properties. *Materials* **2025**, *18*, 3964. [CrossRef] [PubMed]
27. Bartolomeu, R.; Bértolo, R.; Casale, S.; Fernandes, A.; Henriques, C.; Da Costa, P.; Ribeiro, F. Particular Characteristics of Silver Species on Ag-Exchanged LTL Zeolite in K and H Form. *Microporous Mesoporous Mater.* **2013**, *169*, 137–147. [CrossRef]
28. Saidi, M.; Bihl, F.; Gimello, O.; Louis, B.; Roger, A.-C.; Trens, P.; Salles, F. Evaluation of the Hydrophilic/Hydrophobic Balance of 13X Zeolite by Adsorption of Water, Methanol, and Cyclohexane as Pure Vapors or as Mixtures. *Nanomaterials* **2024**, *14*, 213. [CrossRef] [PubMed]
29. Dong, S.; Zhang, B.; Wahiduzzaman, M.; Yang, C.; Liu, Q.; Maurin, G.; Xiong, S.; Wang, S.; Wang, X. Krypton/Xenon Separation at Room Temperature in a Flexible Coordinative Framework Sorbent. *Nat. Commun.* **2026**, *17*, 1065. [CrossRef] [PubMed]

30. Aspromonte, S.G.; Mizrahi, M.D.; Schneeberger, F.A.; López, J.M.R.; Boix, A.V. Study of the Nature and Location of Silver in Ag-Exchanged Mordenite Catalysts. Characterization by Spectroscopic Techniques. *J. Phys. Chem. C* **2013**, *117*, 25433–25442. [CrossRef]
31. Wagner, C.D. Chemical Shifts of Auger Lines, and the Auger Parameter. *Faraday Discuss. Chem. Soc.* **1975**, *60*, 291. [CrossRef]
32. Fonseca, A.M.; Neves, I.C. Study of Silver Species Stabilized in Different Microporous Zeolites. *Microporous Mesoporous Mater.* **2013**, *181*, 83–87. [CrossRef]
33. Shimizu, K.; Sugino, K.; Kato, K.; Yokota, S.; Okumura, K.; Satsuma, A. Formation and Redispersion of Silver Clusters in Ag-MFI Zeolite as Investigated by Time-Resolved QXAFS and UV-Vis. *J. Phys. Chem. C* **2007**, *111*, 1683–1688. [CrossRef]
34. Sánchez-López, P.; Hernández-Hernández, K.A.; Fuentes Moyado, S.; Cadena Nava, R.D.; Smolentseva, E. Antimicrobial and Virus Adsorption Properties of Y-Zeolite Exchanged with Silver and Zinc Cations. *ACS Omega* **2024**, *9*, 7554–7563. [CrossRef] [PubMed]
35. Lopes, C.W.; Martinez-Ortigosa, J.; Góra-Marek, K.; Tarach, K.; Vidal-Moya, J.A.; Palomares, A.E.; Agostini, G.; Blasco, T.; Rey, F. Zeolite-Driven Ag Species during Redox Treatments and Catalytic Implications for SCO of NH_3. *J. Mater. Chem. A* **2021**, *9*, 27448–27458. [CrossRef]
36. Bogdanchikova, N.E.; Dulin, M.N.; Toktarev, A.V.; Shevnina, G.B.; Kolomiichuk, V.N.; Zaikovskii, V.I. Effect of Zeolite Matrix Structure on the Stabilization of Silver Clusters. *React. Kinet. Catal. Lett.* **1993**, *49*, 87–94. [CrossRef]
37. Ozin, G.A.; Hugues, F.; Mattar, S.M.; McIntosh, D.F. Low Nuclearity Silver Clusters in Faujasite-Type Zeolites: Optical Spectroscopy, Photochemistry and Relationship to the Photodimerization of Alkanes. *J. Phys. Chem.* **1983**, *87*, 3445–3450. [CrossRef]
38. Ozin, G.A.; Hugues, F. Silver Atoms and Small Silver Clusters Stabilized in Zeolite Y: Optical Spectroscopy. *J. Phys. Chem.* **1983**, *87*, 94–97. [CrossRef]
39. Sayah, E.; Brouri, D.; Massiani, P. A Comparative in Situ TEM and UV-Visible Spectroscopic Study of the Thermal Evolution of Ag Species Dispersed on Al_2O_3 and NaX Zeolite Supports. *Catal. Today* **2013**, *218–219*, 10–17. [CrossRef]
40. De Cremer, G.; Antoku, Y.; Roeffaers, M.B.J.; Sliwa, M.; Van Noyen, J.; Smout, S.; Hofkens, J.; De Vos, D.E.; Sels, B.F.; Vosch, T. Photoactivation of Silver-Exchanged Zeolite A. *Angew. Chem. Int. Ed.* **2008**, *47*, 2813–2816. [CrossRef] [PubMed]
41. Michalik, J.; Kevan, L. Paramagnetic Silver Clusters in Ag-NaA Zeolite: Electron Spin Resonance and Diffuse Reflectance Spectroscopic Studies. *J. Am. Chem. Soc.* **1986**, *108*, 4247–4253. [CrossRef]
42. Sircar, S.; Mohr, R.; Ristic, C.; Rao, M.B. Isosteric Heat of Adsorption: Theory and Experiment. *J. Phys. Chem. B* **1999**, *103*, 6539–6546. [CrossRef] [PubMed]
43. Al-Muhtaseb, S.A.; Ritter, J.A. New Virial-Type Model for Predicting Single- and Multicomponent Isosteric Heats of Adsorption. *Ind. Eng. Chem. Res.* **1998**, *37*, 684–696. [CrossRef]
44. Swenson, H.; Stadie, N.P. Langmuir's Theory of Adsorption: A Centennial Review. *Langmuir* **2019**, *35*, 5409–5426. [CrossRef] [PubMed]
45. Mathias, P.M.; Kumar, R.; Moyer, J.D.; Schork, J.M.; Srinivasan, S.R.; Auvil, S.R.; Talu, O. Correlation of Multicomponent Gas Adsorption by the Dual-Site Langmuir Model. Application to Nitrogen/Oxygen Adsorption on 5A-Zeolite. *Ind. Eng. Chem. Res.* **1996**, *35*, 2477–2483. [CrossRef]
46. Wang, J.; Wei, Y.; Ma, Z. Modified Dual-Site Langmuir Adsorption Equilibrium Models from A GCMC Molecular Simulation. *Appl. Sci.* **2020**, *10*, 1311. [CrossRef]
47. Dubbeldam, D.; Calero, S.; Ellis, D.E.; Snurr, R.Q. RASPA: Molecular Simulation Software for Adsorption and Diffusion in Flexible Nanoporous Materials. *Mol. Simul.* **2016**, *42*, 81–101. [CrossRef]